The Journal of the Astronautical Sciences (2022) 69:857–878
https://doi.org/10.1007/s40295-022-00316-0

ORIGINAL ARTICLE

Analytical Guidance for Mars Aerocapture via Drag Modulation

Ibrahim H. Cihan[1] · **Craig A. Kluever**[2]

Accepted: 2 March 2022 / Published online: 7 April 2022

Abstract

Aerocapture is a maneuver where a spacecraft makes a single pass through a planetary atmosphere, thus using aerodynamic drag to deplete enough energy to establish a captured orbit. A new analytical predictor-corrector guidance algorithm has been developed for the Mars aerocapture problem. This paper presents a drag-modulation method where ballistic coefficient is continuously adjusted in order to control the vehicle during the atmospheric flight phase. An analytical function for velocity during aerocapture serves as the basis for the guidance method, and this expression results in a closed-form control law for ballistic coefficient. Guidance periodically updates the velocity profile so that the correct exit conditions are achieved. The ballistic coefficient control law utilizes the ratio of the measured and reference drag accelerations to improve the targeting accuracy of the guidance scheme. Two different apoapsis-targeting scenarios for Mars aerocapture are investigated in this paper. Monte Carlo simulations demonstrate the performance and robustness of the proposed guidance algorithm.

Keywords Analytical predictor-corrector · Mars aerocapture · Drag modulation

1 Introduction

Aerocapture is a maneuver where a spacecraft enters a planet's atmosphere at a hyperbolic speed and achieves a captured orbit after a single atmospheric pass. Aerodynamic drag dissipates the vehicle's energy so that the atmospheric exit

✉ Ibrahim H. Cihan
ibrahimcihan@tarsus.edu.tr

Craig A. Kluever
klueverc@missouri.edu

[1] Aerospace Engineering, Faculty of Aeronautics and Astronautics, Tarsus University, Tarsus, Mersin, Turkey

[2] Mechanical and Aerospace Engineering, University of Missouri, MO 65211 Columbia, USA

state results in a closed orbit about the planet. Figure 1 presents a typical scenario for Mars aerocapture. If the aerocapture maneuver is correctly planned, then the apoapsis of the exoatmospheric transfer orbit matches the apoapsis of the target orbit (see Fig. 1). Upon reaching apoapsis, a single impulsive ΔV maneuver raises periapsis to its targeted value.

When compared to an all-propulsive maneuver for establishing the target orbit, aerocapture saves significant propellant mass. Therefore, either more payload mass can be delivered to the target orbit, or a smaller launch vehicle could be used [1–3]. Aerocapture is a promising technology for future interplanetary missions due to its low-cost orbital insertion.

During the atmospheric flight phase, the spacecraft can be controlled by lift-modulation (via bank angle and/or angle of attack) or drag-modulation systems. For guidance designs using lift-modulation, the spacecraft's vertical lift component is adjusted so that the vehicle achieves the correct exit conditions. References [4–7] present guidance schemes that use lift-modulation for aerocapture problems. Lu et al. [4] proposed the optimal bang-bang bank angle control for the Earth aerocapture problem, while Webb et al. [5] investigated Mars aerocapture problems. Both [4, 5] attempt to minimize the post-exit velocity increment ΔV by employing a closed-loop numerical predictor-corrector (NPC) guidance scheme. By definition, NPC schemes predict the atmospheric exit state by using onboard numerical integration of the equations of motion for the atmospheric flight phase. Hence, the control program (usually bank angle) must be parameterized and corrected until the numerical integration produces the desired exit state. Lafleur [6] investigated an apoapsis-targeting mode by seeking a constant bank angle profile in the NPC scheme.

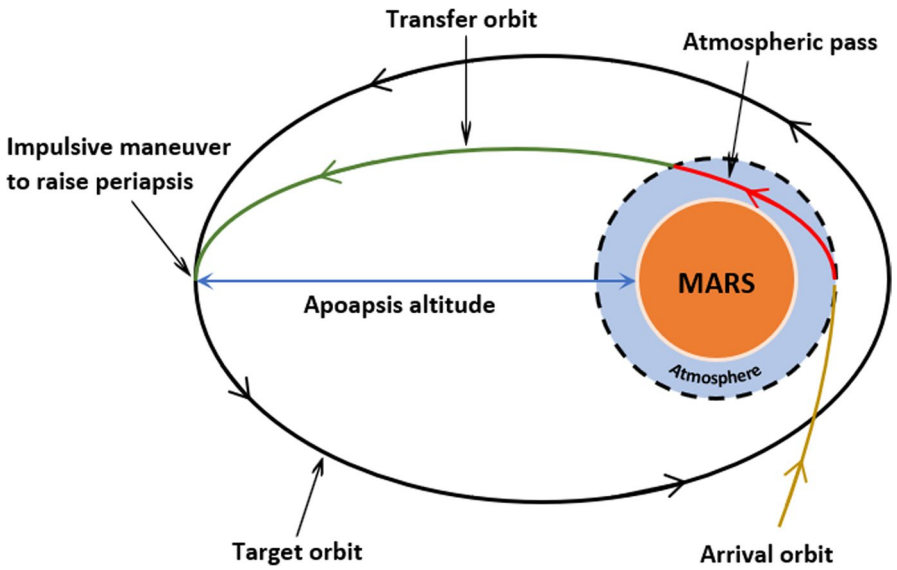

Fig. 1 Mars aerocapture scenario

On the other hand, analytical predictor-corrector (APC) schemes use analytical functions to predict the exit state. Cihan and Kluever [7] developed an APC method for the Earth aerocapture problem where the bank angle is computed from analytical functions for velocity and flight-path angle (FPA) as a function of altitude. References [8–14] present various APC guidance methods for the Mars aerocapture problem with lift (bank angle) modulation as the control function. Many of these methods utilize a two-phase approach, where the initial phase involves equilibrium glide at a constant flight-path angle (FPA), and the second phase tracked a constant altitude-rate profile to exit conditions. Rousseau [14] developed an APC method for Mars aerocapture that was based on the predicted energy at exit conditions.

By comparison, fewer researchers have investigated guidance designs for the ballistic aerocapture problem. In the ballistic scenario, the aerodynamic lift force is zero, and altering aerodynamic drag is the only option for controlling the flight path. Drag force can be modulated during flight by changing the reference area or drag coefficient. Various drag-modulation aerocapture guidance designs have been developed [15–20]. Cihan and Kluever [15] proposed an APC guidance scheme that uses continuous drag-modulation for Mars aerocapture. Recently, Peng et al. presented two different APC guidance algorithms based on continuous drag control [16] and the drag-switching control [17] for Mars aerocapture. In Ref. [16], Peng et al. utilized piecewise linear functions to parameterize velocity during the aerocapture maneuver. Peng et al. used three linear segments to represent velocity as a function of flight-path angle. In Ref. [17], piecewise constant ballistic coefficients are used in the guidance algorithm, and ballistic coefficient switching between these constant values occurs when the analytical prediction of atmospheric exit velocity is equal to the desired exit velocity. Putnam and Braun [18] compared the performance of drag-modulation schemes including single-stage jettison, two-stage jettison, and continuous drag control for planetary missions by using an NPC guidance system for a hypersonic inflatable aerodynamic device (HIAD). Putnam and Braun show that the continuous drag-modulation method provides better accuracy when compared to the single- and two-stage jettison concepts for drag control. Han et al. [20] analyzed the bang-bang ballistic coefficient control for Mars aerocapture. They evaluated four different bang-bang structures for ballistic coefficient and concluded that the four scenarios have nearly the same performance in terms of post-exit ΔV.

This paper presents a novel APC guidance method for Mars aerocapture. Velocity during aerocapture is modeled by a single analytical function (a hyperbolic tangent function) of flight-path angle. This formulation results in a closed-form guidance equation for the commanded ballistic coefficient that tracks the analytic velocity equation. Our algorithm differs from the APC guidance method proposed in Ref. [16] in several ways: 1) the guidance design in this paper is based on a single analytic function for velocity, 2) guidance periodically updates the analytic velocity expression in order to meet the desired boundary conditions, and 3) a drag acceleration correction factor is included to offset the severe uncertainties in Mars' atmospheric density. Furthermore, our method is tested using the Mars Global Reference Atmospheric Model (GRAM), whereas Peng et al. [16] used an exponential density model with variations in scale height. We test our

APC guidance using Monte Carlo simulations for a wide range of entry speeds and two target orbits with very different apoapsis altitudes.

2 System Models

2.1 Equations of Motion for Drag Modulation Flight

During atmospheric flight the spacecraft's equations of motion are

$$\dot{r} = V \sin\gamma \tag{1}$$

$$\dot{\theta} = \frac{V \cos\gamma \sin\psi}{r \cos\phi} \tag{2}$$

$$\dot{\phi} = \frac{V \cos\gamma \cos\psi}{r} \tag{3}$$

$$\dot{V} = -D - g_r \sin\gamma - g_\phi \cos\gamma \cos\psi + \omega^2 r \cos\phi(\sin\gamma \cos\phi - \cos\gamma \cos\psi \sin\phi) \tag{4}$$

$$\dot{\gamma} = \frac{1}{V}\left[\left(\frac{V^2}{r} - g_r\right)\cos\gamma + g_\phi \sin\gamma \cos\psi + 2\omega V \sin\psi \cos\phi + \omega^2 r \cos\phi(\cos\gamma \cos\phi + \sin\gamma \cos\psi \sin\phi)\right] \tag{5}$$

$$\dot{\psi} = \frac{1}{V}\left[\left(\frac{(V\cos\gamma)^2 \tan\phi}{r} + g_\phi\right)\frac{\sin\psi}{\cos\gamma} - 2\omega V(\tan\gamma \cos\psi \cos\phi - \sin\phi) + \frac{\omega^2 r}{\cos\gamma}\sin\psi \sin\phi \cos\phi)\right] \tag{6}$$

where r is the radial distance from the center of the planet to the vehicle's center of mass, θ is the longitude, ϕ is the latitude, V is the planet-relative velocity, γ and ψ are the flight-path and heading angles of the planet-relative velocity vector, respectively, and ω is Mars' rotation rate. The aerodynamic drag acceleration D is

$$D = \frac{1}{2\beta}\rho V^2 \tag{7}$$

where ρ is the atmospheric density and β is the ballistic coefficient

$$\beta = \frac{m}{C_D S} \tag{8}$$

Spacecraft mass is m, C_D is the drag coefficient, and S is the reference area. We assume that Mars' atmosphere rotates with the planet so that the planet-relative velocity V can be used to compute drag in Eq. (7). The radial and latitudinal components of the acceleration of gravity $g_r$and g_ϕ in Eqs. (4–6) are

$$g_r = \frac{\mu}{r^2}\left[1 + J_2\left(\frac{R_m}{r}\right)^2\left(1.5 - 4.5\sin^2\phi\right)\right] \tag{9}$$

$$g_\phi = \frac{3\mu}{r^2}J_2\left(\frac{R_m}{r}\right)^2 \sin\phi\cos\phi \tag{10}$$

where μ is Mars' gravitational parameter, R_m is Mars' equatorial radius, and J_2 is the second zonal coefficient.

Inertial velocity is needed to compute exoatmospheric orbital maneuvers. The spacecraft's inertial velocity vector $\mathbf{V}_i$ is equal to the sum of the planet-relative velocity vector $\mathbf{V}$ and the transport velocity vector $\boldsymbol{\omega}\times\mathbf{r}$.

$$\mathbf{V}_i = \mathbf{V} + \boldsymbol{\omega}\times\mathbf{r}$$

2.2 Exoatmospheric Orbital Transfer

After the spacecraft has exited the atmosphere, it can be transferred from one orbit to another by propulsive maneuvers, which are modeled as impulsive velocity increments without change in orbital position. In order to establish a desired elliptical orbit, one or two in-plane propulsive burns are needed during the exoatmospheric flight phase. When the apoapsis radius of the post-aerocapture orbit is equal to the target apoapsis radius, a single propulsive burn is required to raise periapsis and place the spacecraft in the desired target orbit. In this scenario, the single velocity increment ΔV is

$$\Delta V = \sqrt{2\mu}\left(\sqrt{\frac{1}{r_{a1}} - \frac{1}{r_{p1}+r_{a1}}} - \sqrt{\frac{1}{r_{a0}} - \frac{1}{r_{p0}+r_{a0}}}\right) \tag{11}$$

where r_{a1} and r_{p1} are the apoapsis and periapsis radii of the desired target elliptical orbit, and r_{a0} and r_{p0} are the exoatmospheric apoapsis and periapsis radii, determined by

$$r_{a0} = a\left(1 + \sqrt{1 - \frac{r_{\text{exit}}^2 V_{\text{exit}}^2 \cos^2\gamma_{\text{exit}}}{\mu a}}\right) \tag{12}$$

$$r_{p0} = a\left(1 - \sqrt{1 - \frac{r_{\text{exit}}^2 V_{\text{exit}}^2 \cos^2\gamma_{\text{exit}}}{\mu a}}\right) \tag{13}$$

In Eqs. (12) and (13) r_{exit}, V_{exit}, and γ_{exit} are the radius, inertial velocity, and flight-path angle at the atmospheric exit. Semimajor axis of the exoatmospheric orbit a is determined by the total mechanical energy evaluated at the exit conditions:

$$a = \frac{\mu}{-V_{\text{exit}}^2 + 2\mu/r_{\text{exit}}} \tag{14}$$

If the post-aerocapture apoapsis radius does not equal the desired apoapsis, a two-burn maneuver is needed to establish the target orbit. For both the one- or two-impulse maneuver, the first burn is performed at apoapsis in order to raise periapsis and meet the target r_{p1}. Therefore, the velocity increment for the first burn is always positive. One-half revolution after the first impulse, the vehicle reaches the target periapsis, and a second burn is performed if the apoapsis radius needs correction (the second impulse raises or lowers the apoapsis as needed). The sum of the velocity increments for the two impulses is

$$\Delta V = \sqrt{2\mu}\left(\sqrt{\frac{1}{r_{a0}} - \frac{1}{r_{p1}+r_{a0}}} - \sqrt{\frac{1}{r_{a0}} - \frac{1}{r_{p0}+r_{a0}}}\right) + \sqrt{2\mu}\left|\sqrt{\frac{1}{r_{p1}} - \frac{1}{r_{p1}+r_{a1}}} - \sqrt{\frac{1}{r_{p1}} - \frac{1}{r_{p1}+r_{a0}}}\right| \tag{15}$$

It should be noted that the absolute value is required for the second right-hand side term in Eq. (15) because the initial apoapsis may be greater or less than the target value.

3 Reference Aerocapture Trajectories

This study utilizes a large HIAD that could be used for the human exploration of Mars. The deceleration device has mass m = 45,000 kg. Ballistic coefficient β is the only control variable in this aerocapture problem, and it can be altered by inflating (to make β smaller) or deflating the device (to make β larger). The minimum ballistic coefficient is $\beta_{\min} = 100$ kg/m^2 when the vehicle has maximum diameter $d_{\max} = 18.8$ m and maximum drag coefficient $C_{D,\max} = 1.62$ [16, 17, 21]. The minimum diameter $d_{\min} = 7$ m and corresponding minimum drag coefficient $C_{D,\min} = 1.46$ result in the maximum ballistic coefficient $\beta_{\max} = 800$ kg/m^2.

Table 1 shows two different target elliptical orbits. The first case in Table 1 is known as a 1-sol orbit [5, 22], and the second case is a much lower-energy target [16]. Three different nominal entry velocities were used for all cases: $V_0 = 7.2$, 6.5, and 5.8 km/s. These three values span a range of entry velocities for recent Mars missions that used a direct entry, descent, and landing (EDL) profile, such as Mars Pathfinder ($V_0 = 7.26$ km/s [23]) and Mars Curiosity ($V_0 = 5.8$ km/s, [24]).

The entry FPA angle is a free design variable for any EDL mission (entry velocity, on the other hand, is primarily determined by the departure date and Earth-Mars geometry). In this study, we determined the nominal entry flight-path angle for each entry velocity so that the target apoapsis is achieved with a *constant* ballistic coefficient.

Table 1 Desired Post-Aerocapture Target Orbits

Case	Apoapsis altitude (km)	Periapsis altitude (km)
1	33,793	250
2	3000	250

Table 2 Nominal Entry Velocity and Flight-Path Angle for Constant-β Trajectories

Desired target orbits	Entry velocity (km/s)	Entry flight-path angle (deg)
Case 1a	7.2	−11.420
Case 1b	6.5	−10.864
Case 1c	5.8	−10.071
Case 2a	7.2	−11.556
Case 2b	6.5	−11.031
Case 2c	5.8	−10.295

Table 3 Nominal Entry States

State	Value
Radius	3522 km
Longitude	5 deg
Latitude	5 deg
Inertial heading angle	20 deg

These constant-β aerocapture paths will serve as the reference profile for the guidance design. As such, it makes sense to determine the entry states for a vehicle with a constant ballistic coefficient between $\beta_{\min}$ and $\beta_{\max}$. Although the average value (β=450 kg/m^2) is an obvious first choice, it is not the best choice because the HIAD vehicle requires extra drag margin due to loss of control authority as it approaches the exit (vacuum) condition. Our initial guidance trials produced premature control saturation at $\beta=\beta_{\min}$ (maximum drag) during the ascent phase as the atmosphere gets thinner with increasing altitude. Hence, we selected β_{nom}=350 kg/m^2 as the constant (nominal) ballistic coefficient so that the reference aerocapture trajectories were biased toward a higher drag configuration. The correct entry FPA angle was determined by simulation trials involving numerical integration of Eqs. (1–6) with constant β_{nom}=350 kg/m^2 and a nominal Mars-GRAM density model [25] (the nominal Mars atmosphere was computed by the mean of a 1000 dispersed atmospheres; atmospheric dispersions are discussed in Section 5). Entry FPA was adjusted until the apoapsis of the exoatmospheric orbit exactly matched the target apoapsis values shown in Table 1. Table 2 shows the combinations of nominal entry states (velocity and FPA) for Cases 1 and 2 with constant β_{nom}=350 kg/m^2. For comparison, the entry flight-path angles for EDL missions such as Mars Pathfinder (V_0 =7.26 km/s) and Mars Curiosity (V_0 =5.8 km/s) were − 14.1 and − 15.5 deg, respectively [23, 24] (in general, an EDL mission requires a steeper entry angle when compared to an aerocapture maneuver). Finally, Table 3 presents the remaining entry states (radius, longitude, latitude, and heading angle) that are common for all cases [16, 17].

Figure 2 shows the inertial velocity vs. flight-path angle profiles for the nominal aerocapture trajectories using constant β_{nom}=350 kg/m^2 and the entry states from Tables 2 and 3. Each solid curve in Fig. 2 represents the nominal trajectory determined

by numerical integrating Eqs. (1–6) with the nominal Mars-GRAM density model. Note that each nominal trajectory exits Mars' atmosphere with the correct states such that the apoapsis meets the desired target. Figure 2 shows that Case 1 (1-sol orbit) requires an exit velocity and FPA that is significantly greater than the low-energy target (Case 2).

The inertial velocity of the numerically integrated trajectories in Fig. 2 can be parameterized by a hyperbolic tangent function of flight-path angle

$$V = c_0 + c_1 \tanh\left(c_2 \gamma\right) \tag{16}$$

where c_0, c_1, and c_2 are constants. Here we used MATLAB's Curve Fitting Toolbox (**cftool**) to determine the coefficients c_0, c_1, and c_2 that produced the best fit with the nominal trajectory data. The dashed-line curves in Fig. 2 show the hyperbolic tangent function fit for each entry scenario and apoapsis target. Figure 2 shows that the hyperbolic tangent function (16) provides a good representation of velocity as a function of flight-path angle during the aerocapture maneuver. Our analytical aerocapture guidance law uses Eq. (16) to predict the vehicle's states at the atmospheric exit.

4 Aerocapture Guidance Law

The proposed analytical guidance algorithm is developed by using a simplified version of the equations of motion in a vertical plane. Ignoring the Mars oblateness and planet-rotation terms in Eqs. (4) and (5), the simplified equations for velocity and flight-path angle are

$$\dot{V} = -D - g \sin \gamma \tag{17}$$

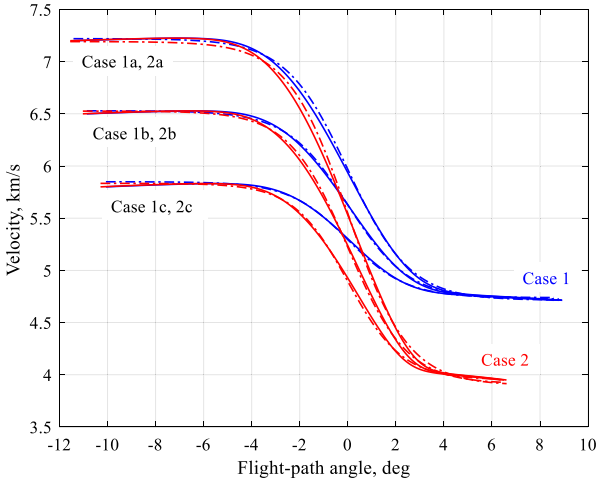

Fig. 2 Reference inertial velocity vs. flight-path angle profiles for constant-β aerocapture trajectories (solid lines are numerically integrated trajectories, dashed lines are curve-fits using Eq. (16))

$$\dot{\gamma} = \frac{1}{V}\left(\frac{V^2}{r} - g\right)\cos\gamma \tag{18}$$

where Mars' gravitational acceleration is $g = \mu/r^2$. The derivative of velocity with respect to flight-path angle is determined by dividing Eqs. (17) by Eq. (18)

$$\frac{dV}{d\gamma} = \frac{-D - g\sin\gamma}{\frac{G\cos\gamma}{V}} \tag{19}$$

where $G = V^2/r - g$. We can take a derivative of the hyperbolic tangent function (16) with respect to flight-path angle to obtain

$$\frac{dV}{d\gamma} = \frac{c_1 c_2}{\cosh^2(c_2\gamma)} \tag{20}$$

After substituting Eq. (16) for velocity in Eq. (19), we can equate Eqs. (19) and (20) and solve for drag acceleration to yield

$$D_{\text{ref}} = \frac{-Gc_1c_2\cos\gamma}{(c_0 + c_1\tanh(c_2\gamma))\cosh^2(c_2\gamma)} - g\sin\gamma \tag{21}$$

Eq. (21) is the reference drag acceleration required to track the reference velocity defined by the hyperbolic tangent function (16). Although the substitution is not explicitly shown here, we must use Eq. (16) to compute the term $G = V^2/r - g$ in Eq. (21). Finally, we can substitute Eqs. (16) and (21) into Eq. (7) and solve for the ballistic coefficient to obtain

$$\beta = \frac{1}{2D_{\text{ref}}}\rho\left(c_0 + c_1\tanh(c_2\gamma)\right)^2 \tag{22}$$

Eq. (22) is the ballistic coefficient required to track Eq. (16). Note that Eq. (22) relies on a model of atmospheric density ρ, which can be uncertain. Hence, the commanded ballistic coefficient can be improved by incorporating a factor that accounts for variations in atmospheric density relative to the nominal model. Here the drag scaling factor is $K_\rho = \hat{D}/D_{\text{ref}}$, where $\hat{D}$ is the measured drag acceleration from the vehicle's onboard sensors. Incorporating this scale factor into Eq. (22) yields the commanded ballistic coefficient

$$\beta_{\text{cmd}} = \frac{1}{2D_{\text{ref}}}K_\rho\rho\left(c_0 + c_1\tanh(c_2\gamma)\right)^2 \tag{23}$$

Eq. (23) requires the coefficients c_0, c_1, and c_2 to compute the ballistic coefficient command. Recall that MATLAB's **cftool** was used to determine these coefficients given the nominal aerocapture trajectories shown in Fig. 2. For the onboard guidance design, we wish to re-fit the velocity vs. FPA profile at periodic guidance updates so that the boundary conditions are satisfied. Hence, in principle, the three unknown coefficients can be determined by solving a system of three equations based on Eq. (16). However, the hyperbolic tangent function is

nonlinear, which complicates an onboard updating scheme because we must solve a system of three nonlinear equations. If we assume that c_2 is a predefined constant, then the system will become much easier to solve. Here we use the value of coefficient c_2 from the curve-fits of the nominal trajectories (Fig. 2). At each guidance update, the two coefficients c_0 and c_1 are determined by the velocity and FPA at the boundary conditions $(V_{\text{now}}, \gamma_{\text{now}})$ and $(V_{\text{tgt}}, \gamma_{\text{tgt}})$. The current states $(V_{\text{now}}, \gamma_{\text{now}})$ are known and determined by the navigation system. We select the target states $(V_{\text{tgt}}, \gamma_{\text{tgt}})$ at an altitude of 80 km from the nominal numerical simulation with a constant ballistic coefficient, $\beta_{\text{nom}} = 350$ kg/m^2. Table 4 presents the targets $(V_{\text{tgt}}, \gamma_{\text{tgt}})$ at 80 km altitude during a nominal ascent phase. By defining $x_{\text{now}} = \tanh(c_2\gamma_{\text{now}})$ and $x_{\text{tgt}} = \tanh(c_2\gamma_{\text{tgt}})$, we create a set of two linear equations by evaluating Eq. (16) at the boundary conditions

$$V_{\text{now}} = c_0 + c_1 x_{\text{now}} \quad \text{and} \quad V_{\text{tgt}} = c_0 + c_1 x_{\text{tgt}} \tag{24}$$

Coefficients c_0 and c_1 are updated at each guidance cycle (frequency is 1 Hz). These coefficients (along with constant coefficient c_2) are used in Eqs. (16) and (23) to determine the commanded ballistic coefficient.

Eq. (23) provides the commanded ballistic coefficient until the current FPA crosses the γ_{tgt} threshold (nominally at 80 km altitude). For the remainder of the ascent trajectory (from the 80-km target state to the 125-km altitude exit state), the commanded ballistic coefficient is a constant determined by

$$\beta_{\text{cmd}} = \beta_{\text{nom}} + \frac{K_1}{V_{\text{tgt}}}\left(V_{\text{tgt}} - V_{\text{TH}}\right) \tag{25}$$

where gain $K_1 = 1.5(10^6)$ kg/m^2 and V_{TH} is the vehicle's velocity when it reaches the targeted FPAγ_{tgt} (the vehicle's flight-path angle will cross γ_{tgt} during the exit phase, but it may not necessarily do so at 80 km altitude and the targeted velocity). We determined that a sufficiently large gain K_1 is needed in Eq. (25) because the targeted velocity at 80 km is usually quite large (see Table 4) and the velocity error is usually less than 5 m/s. In the best-case scenario $V_{\text{TH}} = V_{\text{tgt}}$ at the FPA threshold and the commanded ballistic coefficient is the nominal value (350 kg/m^2) for the remainder of the flight to atmospheric exit. For over- and under-speed conditions, the ballistic coefficient is adjusted (and often saturated at its minimum or maximum value)

Table 4 Nominal Velocity and Flight-Path Angle Targets during Ascent (80-km Altitude)

Mars target orbit	Velocity V_{tgt} (km/s)	Flight-path angle γ_{tgt} (deg)
Case 1a	4.748	6.46
Case 1b	4.748	6.25
Case 1c	4.748	5.95
Case 2a	3.972	5.77
Case 2b	3.972	5.64
Case 2c	3.972	5.48

Table 5 Predefined c_2 Coefficient for the Hyperbolic Tangent Function

Desired target orbits	c_2
Case 1a	−22.17
Case 1b	−22.45
Case 1c	−23.45
Case 2a	−22.85
Case 2b	−23.35
Case 2c	−25.21

Table 6 Entry State Error Dispersions

State	Distribution	Dispersion
Longitude	Gaussian	$3\sigma = 0.05$ deg
Latitude	Gaussian	$3\sigma = 0.05$ deg
Inertial velocity	Gaussian	$3\sigma = 20$ m/s
Inertial flight-path angle	Gaussian	$3\sigma = 0.1$ deg
Inertial heading angle	Gaussian	$3\sigma = 0.05$ deg

in an attempt to increase or decrease drag in this region of flight where the vehicle has very low control authority due to the thinning atmosphere above 80 km.

5 Aerocapture Guidance Performance

Monte Carlo simulations are executed to evaluate the performance and robustness of the guidance algorithm. Because we have six different entry scenarios (two different post-exit target orbits and three different entry velocities; see Tables 1 and 2), we have six different numerically integrated reference trajectories (see Fig. 2). Thus, we need to compute six different hyperbolic tangent coefficients c_2 using cftool and the appropriate reference velocity vs. FPA profile. Table 5 presents the coefficient values for all six scenarios.

The Monte Carlo simulation involves dispersions in the entry states. All entry states (except radius) are randomly dispersed about their nominal values using zero-mean Gaussian distributions. Table 6 presents their 3σ dispersion values. The vehicle's actual ballistic coefficient used in the numerical simulations is equal to a lagged value of commanded ballistic coefficient with a time constant of 0.25 s. We assume that uncertainties in the drag coefficient, HIAD area, and mass result in a random error in ballistic coefficient with a zero mean and 3σ dispersion of 15%. In addition, the maximum ballistic coefficient actuation rate is limited to 30 kg/m^2-s. We assume perfect state feedback for our guidance laws. Mars-GRAM [25] was used to generate 1000 dispersed atmospheres with density dispersions and atmospheric dust opacity (dusttau) randomly varied with a uniform distribution between 0.1 and 0.9. Fig. 3 shows atmospheric density variation with altitude by presenting the ratios of 1000

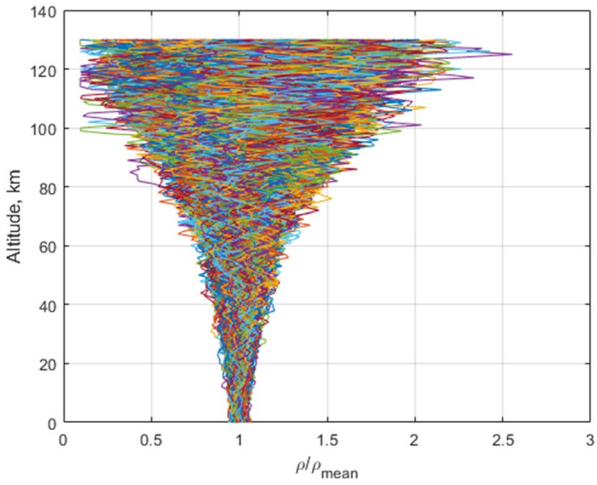

Fig. 3 Dispersed Mars-GRAM density variation with altitude

dispersed density profiles relative to the mean value. Density dispersions vary with longitude and latitude as well as altitude [7].

5.1 Numerical Results for Case 1 (1-sol Target Orbit)

The aerocapture trajectories are generated by numerically integrating Eqs. (1–6) using MATLAB's ode45 solver with a maximum step size of 0.025 s. Atmospheric density is determined by a table look-up of the dispersed atmosphere as a function of altitude. For each case, a 1000-run Monte Carlo simulation is conducted. Figures 4, 5 and 6 and Table 7 present simulation results for the three entry scenarios for Case 1 (the desired target is a 33,793 × 250 km 1-sol orbit). Figure 4 shows that the inertial velocity versus flight-path angle curves for each scenario converge to the

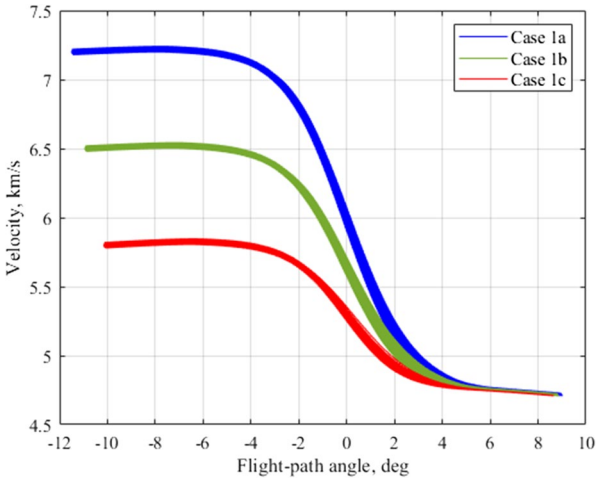

Fig. 4 Velocity vs. flight-path angle for the three 1000-run Monte Carlo simulations of Case 1

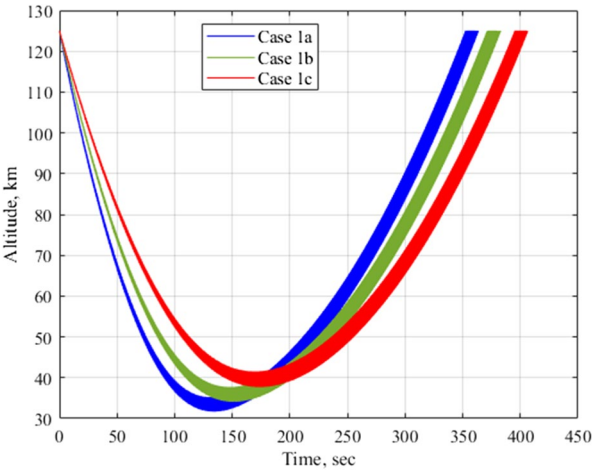

Fig. 5 Altitude vs. time for the three 1000-run Monte Carlo simulations of Case 1

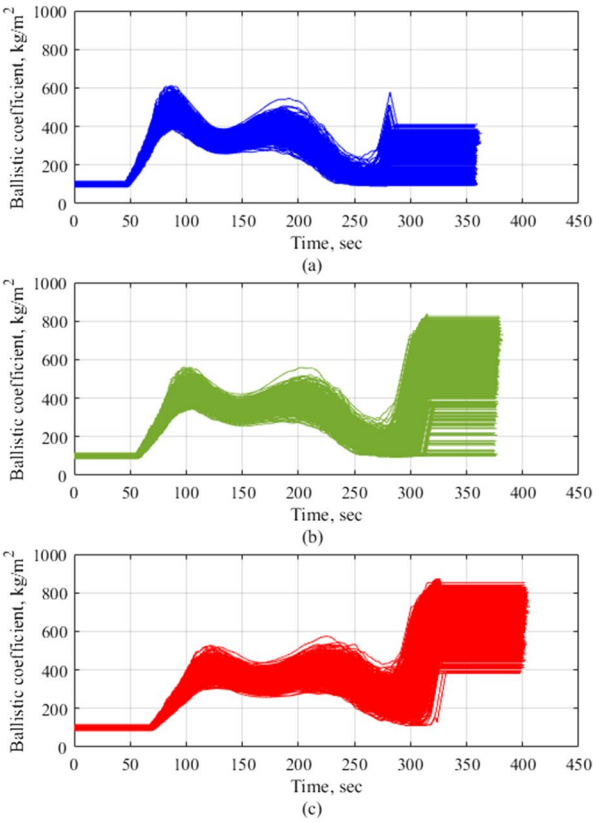

Fig. 6 Ballistic coefficient vs. time for the three 1000-run Monte Carlo simulations of Case 1: **a**) $V_0 = 7.2$ km/s, **b**) $V_0 = 6.5$ km/s, **c**) $V_0 = 5.8$ km/s

Table 7 Monte Carlo Statistical Results for Case 1

Case	Parameter	Mean	Standard deviation	Minimum	Maximum
1a	Apoapsis altitude	33,799.9 km	353.2 km	33,215.9 km	36,697.0 km
	Total ΔV[a]	13.79 m/s	1.44 m/s	12.59 m/s	26.78 m/s
1b	Apoapsis altitude	33,633.9 km	210.6 km	33,077.2 km	35,830.3 km
	Total ΔV[b]	13.65 m/s	0.90 m/s	12.41 m/s	22.65 m/s
1c	Apoapsis altitude	33,602.2 km	135.4 km	33,012.5 km	34,003.0 km
	Total ΔV[c]	13.35 m/s	0.77 m/s	12.14 m/s	16.92 m/s

[a]Total $\Delta V = 12.63$ m/s for nominal entry

[b]Total $\Delta V = 12.44$ m/s for nominal entry

[c]Total $\Delta V = 12.14$ m/s for nominal entry

targeted atmospheric exit state. For the three 1000-run Monte Carlo trials for Case 1, the exit velocity and FPA range from 4.71 to 4.73 km/s and from 8.5 to 9.0 deg, respectively. Figure 5 shows the altitude time histories for the three Monte Carlo simulations. The pull-up altitudes (where FPA = 0) are lowest for the high-speed entry (Case 1a, average pull-up altitude is 33 km) and greatest for the low-speed entry (Case 1c, average pull-up altitude is 40 km).

Figure 6 presents the ballistic coefficient time histories for the 1-sol target orbit. Because the closed-loop ballistic coefficient computed by Eq. (23) is too low during the initial high-altitude entry (due to low atmospheric density), the vehicle flies with a minimum ballistic coefficient for the first 45–70 s in the Case 1 scenarios. During the relatively dense part of the atmosphere (roughly $50 < t < 280$ s, see Fig. 5), the closed-loop guidance law (23) modulates the ballistic coefficient in order to track the updated velocity profile determined by Eq. (16) and the target boundary conditions. After the current FPA exceeds the target threshold (roughly $280 < t < 325$ s), the ballistic coefficient is governed by Eq. (25) and held constant. The commanded

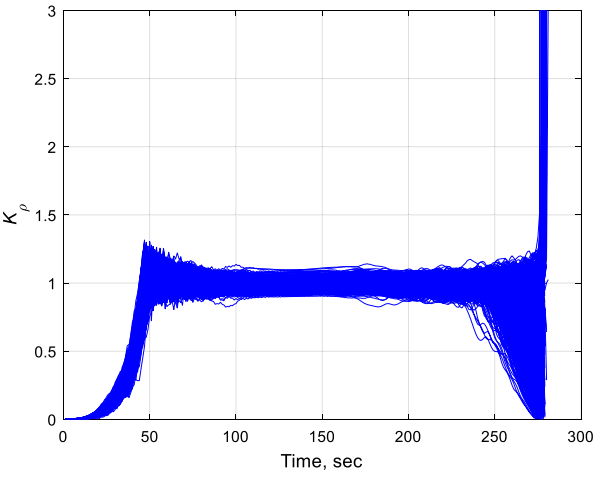

Fig. 7 Measured/reference drag scaling factor $\hat{D}/D_{\text{ref}}$ vs. time for the 1000 Monte Carlo simulations of Case 1a ($V_0 = 7.2$ km/s)

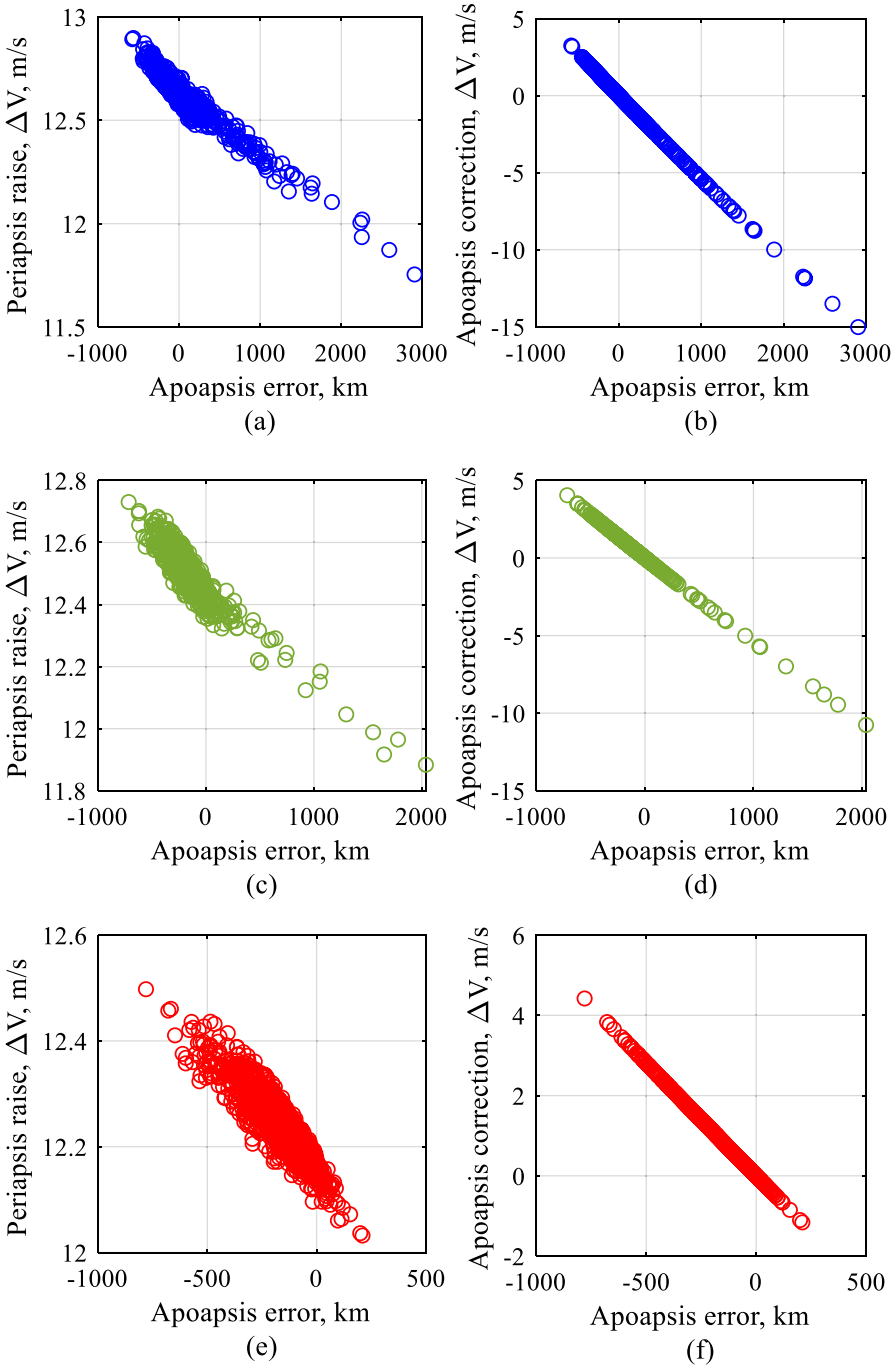

Fig. 8 Impulsive ΔV for the Case 1 Monte Carlo trials: periapsis raise and apoapsis correction maneuvers vs. apoapsis errors (blue = Case 1a, green = Case 1b, red = Case 1c)

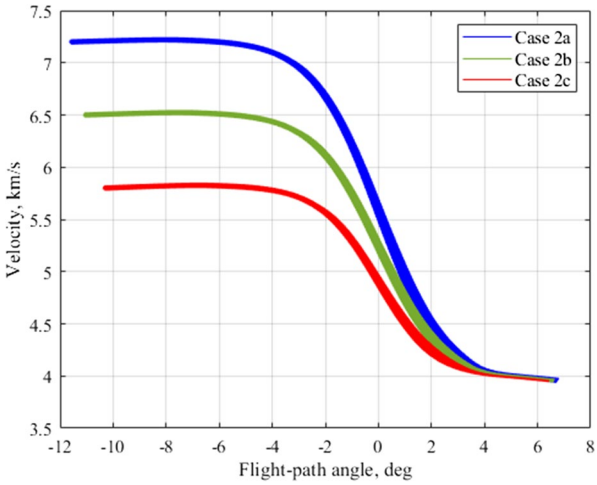

Fig. 9 Velocity vs. flight-path angle for the three 1000-run Monte Carlo simulations of Case 2

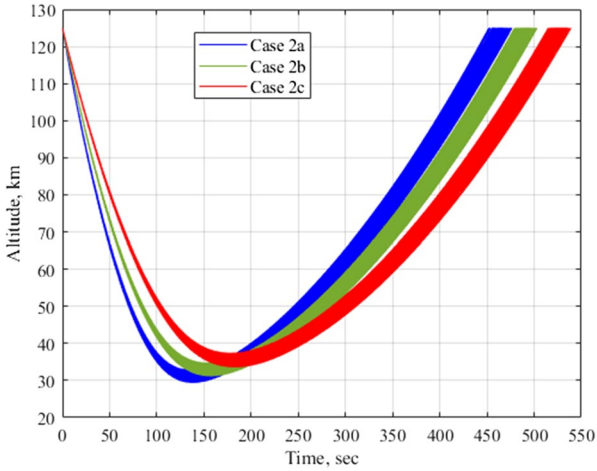

Fig. 10 Altitude vs. time for the three 1000-run Monte Carlo simulations of Case 2

constant ballistic coefficient during the latter part of the exit phase is less than 350 kg/m^2 for most of 1000 trajectories in Case 1a (high-speed entry, Fig. 6a). This strategy brings the apoapsis altitude of the post-aerocapture orbit closer to the target apoapsis. On the other hand, for the low-speed entry (Case 1c, Fig. 6c), the constant ballistic coefficient is larger than the nominal value in order to decrease the drag acceleration during that latter part of the exit phase. Therefore, this increases the exit velocity and the apoapsis altitude of the exo-atmospheric trajectory.

Figure 7 presents the evolution of the drag scaling factor $K_\rho = \hat{D}/D_{\text{ref}}$ (for Case 1a) that is used in the closed-loop ballistic coefficient control law (23). The factor K_ρ is between 0.75 and 1.25 during the dense region of the atmospheric pass

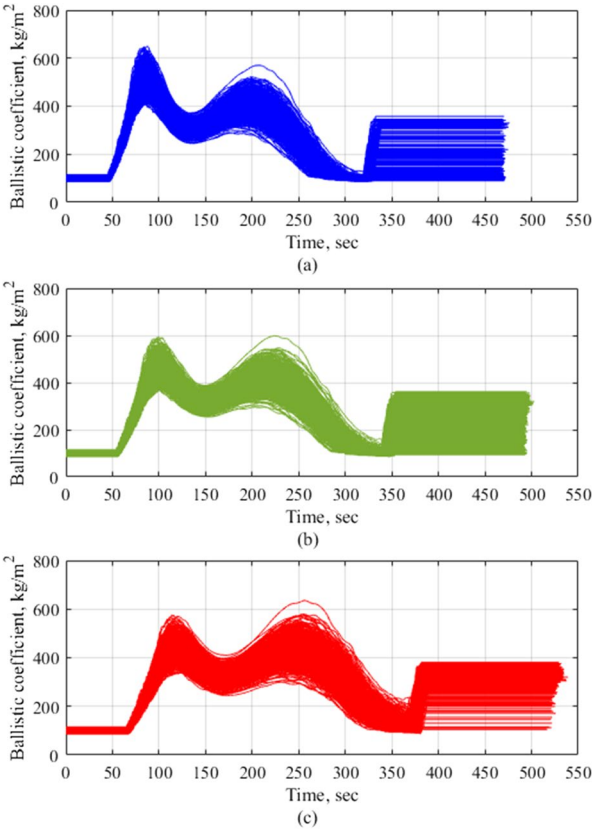

Fig. 11 Ballistic coefficient vs. time for the three 1000-run Monte Carlo simulations of Case 2

(again, roughly $50 < t < 250$ s), and the smallest variation in K_ρ occurs at $t = 140$ s where the vehicle is near its lowest altitude (pull-up). Fig. 7 shows that the scale factor becomes divergent as the vehicle's FPA approaches the γ_{tgt}threshold (at about 80-km altitude) when $t > 250$ s. In this region where atmospheric density is thin, the drag acceleration D_{ref} required to track the reference velocity, Eq. (21), can become dramatically different from an achievable drag acceleration. In cases where D_{ref} becomes unrealistically large, K_ρ becomes small and the ballistic coefficient saturates at its lower bound as shown in Fig. 6a ($t > 250$ s). For the opposite scenario (small D_{ref}), K_ρ becomes large. However, the value of K_ρ has little impact on the exit conditions at these high altitudes because drag modulation has low control authority. When the vehicle crosses the γ_{tgt} threshold ($t > 280$ s), a constant commanded ballistic coefficient is dictated by Eq. (25) instead of Eq. (23) and hence the scale factor K_ρ is no longer used. Here we only show the scale factor for Case 1a; the profiles for K_ρ vs. time are similar for Cases 1b and 1c.

Table 7 summarizes the statistical results of the three 1000-run Monte Carlo trajectories for each entry scenario for Case 1. Mean and standard deviation values of the post-aerocapture apoapsis altitude and total ΔV decrease with diminishing entry velocity (see Table 2 for the three entry scenarios for Case 1). The

Table 8 Monte Carlo Statistical Results for Case 2

Case	Parameter	Mean	Standard deviation	Minimum	Maximum
2a	Apoapsis altitude	3008.8 km	49.85 km	2908.0 km	3257.9 km
	Total ΔV[a]	49.77 m/s	3.48 m/s	45.50 m/s	72.08 m/s
2b	Apoapsis altitude	3001.3 km	26.1 km	2956.7 km	3169.6 km
	Total ΔV[b]	46.74 m/s	2.09 m/s	44.57 m/s	62.45 m/s
2c	Apoapsis altitude	2994.7 km	14.2 km	2959.1 km	3058.4 km
	Total ΔV[c]	45.25 m/s	1.01 m/s	43.59 m/s	50.01 m/s

[a]Total $\Delta V = 45.20$ m/s for nominal entry

[b]Total $\Delta V = 44.41$ m/s for nominal entry

[c]Total $\Delta V = 43.67$ m/s for nominal entry

worst mean exoatmospheric apoapsis altitude is 33,602 km (Case 1c), which is only 191 km below the target value. The maximum exoatmospheric apoapsis altitude out of all three 1000-run trials is 36,697 km, which is 2904 km greater than the target apoapsis altitude. The corresponding total ΔV is 26.78 m/s for this worst case. Although the standard deviations of the post-aerocapture apoapsis altitudes appear to be large (the greatest value is 353.2 km for Case 1a), they represent less than 1% error relative to the targeted apoapsis. The single-burn ΔV values for each nominal entry scenario (using $\beta_{\text{nom}} = 350$ kg/m^2) are 12.63 m/s, 12.44 m/s, and 12.14 m/s, for Cases 1a-1c, respectively. Hence, the mean ΔV values shown in Table 7 are about 1.2 m/s larger than the nominal single-burn ΔV values.

For comparison purposes, we removed the drag scaling factor $K_\rho = \hat{D}/D_{\text{ref}}$ in the ballistic coefficient guidance law (23) and re-ran the Monte Carlo trials. The mean total ΔV increased by as much as 12% (Case 1a) when compared to the results presented in Table 7. Hence, the scale factor K_ρ plays a critical role in enhancing the performance of the proposed guidance algorithm.

Figure 8 shows the ΔV impulses for the three 1000-run Monte Carlo trials for Cases 1a, 1b, and 1c. It is clear that the majority of the total ΔV is comprised of the periapsis-raise burn at the post-aerocapture apoapsis. For the high-speed entry (Case 1a), most apoapsis-correction impulses (applied at periapsis) are less than 5 m/s. For the low-speed entry (Case 1c), the apoapsis-correct impulses become smaller compared to Case 1a.

5.2 Numerical Results for Case 2 (3000-km Apoapsis Target Orbit)

Recall that Case 2 involves an exoatmospheric target orbit with apoapsis and periapsis altitudes of 3000 km and 250 km, respectively (this is the target orbit used by Peng et al. [16]). Relative to Case 1, it is clear that the vehicle must extend the duration of the atmospheric flight phase in order to deplete additional energy and achieve a lower apoapsis target. Figs. 9, 10 and 11 show the

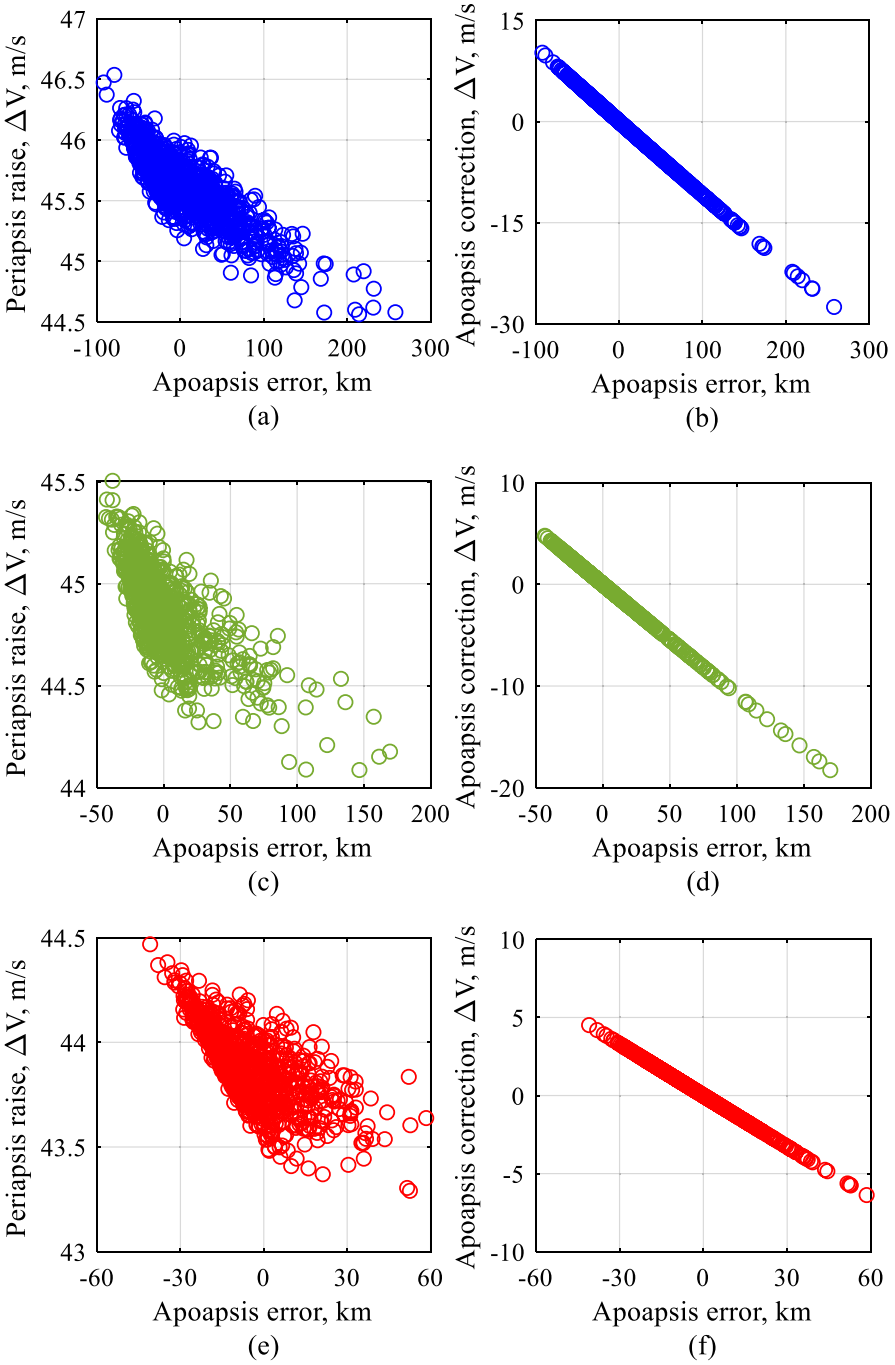

Fig. 12 Impulsive ΔV for the Case 2 Monte Carlo trials: periapsis raise and apoapsis correction maneuvers vs. apoapsis errors (blue = Case 2a, green = Case 2b, red = Case 2c)

trajectories from the three 1000-run Monte Carlo simulations for Case 2. Fig. 9 shows that all trials converge to the same targeted exit states (exit velocity is between 3.94 and 3.98 km/s, while exit FPA is between 6.39 and 6.80 deg). Figure 10 shows that the vehicle's pull-up altitude for Case 2 is lower compared to Case 1; this phenomenon is required to dissipate additional energy before atmospheric exit. Figure 11 shows that the ballistic coefficient modulation follows a time-history profile that is similar to the profiles in Case 1 (Fig. 6). The exception is that the constant-β values for the exit phase above 80-km exhibits little change with entry velocity when compared to Fig. 6.

Table 8 presents the Monte Carlo statistics for Case 2. The single-impulse ΔV values for the nominal entry scenarios (with constant $\beta = 350$ kg/m^2) are 45.20 m/s, 44.41 m/s, and 43.67 m/s for Cases 2a, 2b, and 2c, respectively. Table 8 shows that the mean total ΔV value for the high-speed Monte Carlo simulation (Case 2a) is 5 m/s greater than the nominal value; the two other mean total ΔV values are only about 2 m/s greater than the corresponding nominal aerocapture maneuvers. Table 8 also shows that the guidance algorithm is able to reliably deliver the vehicle to the targeted apoapsis altitude with deviations that are much smaller than those reported in Ref 16. Tables 7 and 8 show that the aerocapture guidance exhibits better performance for the low-speed entry trials, Cases 1c and 2c.

Figure 12 shows the impulsive ΔV values for the periapsis-raise and apoapsis-correction maneuvers. Similar to the Case 1 trials, the majority of the total ΔV occurs at apoapsis for the periapsis-raise maneuver, and the magnitude of the apoapsis-correction impulse decreases with diminishing entry velocity.

6 Conclusions

A new analytical predictor-corrector guidance system has been developed for a ballistic Mars aerocapture maneuver. This guidance scheme employs a drag-modulation law to track a velocity profile that is analytically defined by a hyperbolic tangent function of flight-path angle. Our guidance design periodically updates the reference velocity profile by re-fitting the hyperbolic tangent function to the vehicle's current and target states. This feedback scheme reliably produces the correct atmospheric exit states so that the exoatmospheric phase achieves the target apoapsis altitude. Another key feature of the drag-modulation guidance law is the inclusion of a factor comprised of the ratio of measured and modeled atmospheric drag. This drag scaling factor is essential for robust performance in the presence of Mars' uncertain atmospheric density. The proposed guidance system is successfully demonstrated by Monte Carlo simulations with dispersions in the entry state, density model, and ballistic coefficient. The simulation results reveal that the proposed guidance design is a robust algorithm that provides near-optimal performance in terms of post-exit impulsive ΔV required to establish the desired target orbit.

Declarations

An earlier version of this article was first presented at the 31st AAS/AIAA Space Flight Mechanics Meeting on February 1–3, 2021. The authors declare that they have no known competing financial interests or personal relationships that could have appeared to influence the work reported in this paper.

References

1. Hall, J.L., Noca, M.A., Bailey, R.W.: Cost-benefit analysis of the Aerocapture Mission set. J. Spacecr. Rocket. **42**(2), 309–320 (2005). https://doi.org/10.2514/1.4118
2. Munk, M.M., Moon, S.A.: Aerocapture Technology Development Overview. In: 2008 IEEE Aerospace Conference, pp. 1–7, IEEE (2008). https://doi.org/10.1109/aero.2008.4526545
3. Spilker, T.R., Adler, M., Arora, N., Beauchamp, P.M., Cutts, J.A., Munk, M.M., Powell, R.W., Braun, R.D., Wercinski, P.F.: Qualitative assessment of Aerocapture and applications to future missions. J. Spacecr. Rocket. **56**(2), 536–545 (2019). https://doi.org/10.2514/1.a34056
4. Lu, P., Cerimele, C.J., Tigges, M.A., Matz, D.A.: Optimal Aerocapture Guidance. J. Guid. Control. Dyn. **38**(4), 553–565 (2015). https://doi.org/10.2514/1.G000713
5. Webb, K.D., Lu, P., Dwyer Cianciolo, A.M.: Aerocapture Guidance for a Human Mars Mission. In: AIAA Guidance, Navigation, and Control Conference, AIAA 2017-1900 (2017). https://doi.org/10.2514/6.2017-1900
6. Lafleur, J.M.: The conditional equivalence of ΔV minimization and apoapsis targeting in numerical predictor-corrector aerocapture guidance. Tech rep. NASA/TM-2011-216156. Johnson Space Center, Houston (2011)
7. Cihan, I.H., Kluever, C.A.: Analytical Earth-aerocapture guidance with near-optimal performance. J. Guid. Control. Dyn. **44**(1), 45–56 (2021). https://doi.org/10.2514/1.G005229
8. Gamble, J.D., Cerimele, C.J., Moore, T.E., Higgins, J.: Atmospheric guidance concepts for an aeroassisted flight experiment. J. Astronaut. Sci. **36**(1), 45–71 (1988)
9. Masciarelli, J., Rousseau, S., Fraysse, H., Perot, E.: An analytic aerocapture guidance algorithm for the Mars sample return orbiter. In: AIAA Atmospheric Flight Mechanics Conference, Denver, Colorado, USA, AIAA 2000-4116 (2000). https://doi.org/10.2514/6.2000-4116
10. Masciarelli, J.: Aerocapture Guidance Algorithm Development and Testing. In: 2007 NASA Science Technology Conference, College Park, MD, USA (2007)
11. Hanak, C., Crain, T., Masciarelli, J.: Revised Algorithm for Analytic Predictor-Corrector Aerocapture Guidance: Exit Phase. In: AIAA Guidance, Navigation, and Control Conference, Austin, TX, USA, AIAA 2003-5746 (2003). https://doi.org/10.2514/6.2003-5746
12. Rousseau, S., Perot, E., Graves, C., Masciarelli, J., Queen, E.: Aerocapture Guidance Algorithm Comparison Campaign. In: AIAA/AAS Astrodynamics Specialist Conference and Exhibit, Monterey, CA, USA, AIAA 2002-4822 (2002). https://doi.org/10.2514/6.2002-4822
13. Hamel, J.-F., Lafontaine, J.D.: Improvement to the analytical predictor-corrector guidance algorithm applied to Mars aerocapture. J. Guid. Control. Dyn. **29**(4), 1019–1022 (2006). https://doi.org/10.2514/1.20126
14. Rousseau, S.: An Energy Controller Aerocapture Guidance Algorithm for the Mars Sample Return Orbiter. In: 2001 AAS/AIAA Space Flight Mechanics Meeting, Santa Barbara, CA, USA, AAS 01-104 (2001)
15. Cihan, I. H., Kluever, C. A.: Analytical Guidance for Mars Aerocapture via Drag Modulation. In: 31st AAS/AIAA Space Flight Mechanics Meeting, Virtual, AAS 21-308 (2021)
16. Peng, Y.M., Xu, B., Fang, B.D., Lei, H.L.: Analytical predictor-corrector guidance algorithm based on drag modulation flight control system for Mars aerocapture. Int. J. Aerosp. Eng. **2018**, 1–12 (2018). https://doi.org/10.1155/2018/5907981
17. Peng, Y.M., Xu, B., Lu, X., Fang, B.D., Zhang, H.: Analytical predictive guidance algorithm based on single ballistic coefficient switching for Mars aerocapture. Int. J. Aerosp. Eng. **2019**, 1–9 (2019). https://doi.org/10.1155/2019/5765901
18. Putnam, Z.R.L., Braun, R.D.: Drag-modulation flight-control system options for planetary aerocapture. J Spacecr Rocket **51**(1), 139–150 (2014). https://doi.org/10.2514/1.A32589
19. Putnam, Z.R.L., Clark, I.G., Braun, R.D.: Drag Modulation Flight Control for Aerocapture. In: 2012 IEEE Aerospace Conference, pp. 1–10 (2012). https://doi.org/10.1109/aero.2012.6186999

20. Han, H., Qiao, D., Chen, H.: Optimal Ballistic Coefficient Control for Mars Aerocapture. In: 2016 IEEE Chinese Guidance, Navigation and Control Conference (CGNCC), pp. 2175–2180 (2016). https://doi.org/10.1109/cgncc.2016.7829129
21. Polsgrove, T., Chapman, J., Sutherlin, S., Taylor, B., Robertson, E., Studak, B., Vitalpur, S., Fabisinski, L., Lee, A.Y., Collins, T., Cianciolo, A.D.: Human Mars Lander Design for NASA's Evolvable Mars Campaign. 2016 IEEE Aerospace Conference, pp. 1–15 (2016). https://doi.org/10.1109/aero.2016.7500778
22. Davis, J., Dwyer Cianciolo, A., Powell, R., Shidner, J., García-Llama, E.: Guidance and control algorithms for the Mars entry, descent and landing systems analysis. In: AIAA Astrodynamics Specialist Conference, Toronto, Canada, AIAA 2010-7972 (2010). https://doi.org/10.2514/6.2010-7972
23. Spencer, D. A., Blanchard, R. C., Thurman, S. W., Braun, R. D., Peng, C. Y., Kallemeyn, P. H.: Mars pathfinder atmospheric entry reconstruction. In: 1998 AAS/AIAA Space Flight Mechanics Meeting, Monterey, CA, USA, AAS 98-146 (1998)
24. Kornfeld, R.P., Prakash, R., Devereaux, A.S., Greco, M.E., Harmon, C.C., Kipp, D.M.: Verification and validation of the Mars science laboratory/Curiosity rover entry, descent, and landing system. J. Spacecr. Rocket. **51**(4), 1251–1269 (2014). https://doi.org/10.2514/1.a32680
25. Mars Global Reference Atmospheric Model 2010 (Mars GRAM 2010). https://software.nasa.gov/software/MFS-33158-1. Accessed January 2020